PHYSICAL REVIEW MATERIALS **2**, 054407 (2018)

Effect of *in situ* electric-field-assisted growth on antiphase boundaries in epitaxial Fe_3O_4 thin films on MgO

Ankit Kumar,[1,*] Erik Wetterskog,[1] Erik Lewin,[2] Cheuk-Wai Tai,[3] Serkan Akansel,[1] Sajid Husain,[4] Tomas Edvinsson,[1]
Rimantas Brucas,[1] Sujeet Chaudhary,[4] and Peter Svedlindh[1,†]
[1]*Department of Engineering Sciences, Uppsala University, Box 534, SE-751 21 Uppsala, Sweden*
[2]*Department of Chemistry - Ångström Laboratory, Uppsala University, SE-751 21 Uppsala, Sweden*
[3]*Department of Materials and Environmental Chemistry, Stockholm University, Stockholm, Sweden*
[4]*Department of Physics, Indian Institute of Technology Delhi, New Delhi, India*

(Received 5 January 2018; revised manuscript received 17 April 2018; published 17 May 2018)

Antiphase boundaries (APBs) normally form as a consequence of the initial growth conditions in all spinel ferrite thin films. These boundaries result from the intrinsic nucleation and growth mechanism, and are observed as regions where the periodicity of the crystalline lattice is disrupted. The presence of APBs in epitaxial films of the inverse spinel Fe_3O_4 alters their electronic and magnetic properties due to strong antiferromagnetic (AF) interactions across these boundaries. We explore the effect of using in-plane *in situ* electric-field-assisted growth on the formation of APBs in heteroepitaxial $Fe_3O_4(100)/MgO(100)$ thin films. The electric-field-assisted growth is found to reduce the AF interactions across APBs and, as a consequence, APB-free thin-film-like properties are obtained, which have been probed by electronic, magnetic, and structural characterization. The electric field plays a critical role in controlling the density of APBs during the nucleation process by providing an electrostatic force acting on adatoms and therefore changing their kinetics. This innovative technique can be employed to grow epitaxial spinel thin films with controlled AF interactions across APBs.

DOI: 10.1103/PhysRevMaterials.2.054407

I. INTRODUCTION

Magnetite (Fe_3O_4) is one of the oldest known magnetic materials with a wide range of applications: as magnetoreceptors used by certain organisms to perceive direction [1], as a catalyst in surface science [1], or as magnetic labels in bioassays [1]. In recent years, magnetite has acquired increased interest from researchers not only due to being a strongly correlated electron system but also due to being an attractive material for the nascent field of spintronics because of its half-metallic character, high conductivity ($\sim 250\ \Omega^{-1}\,\mathrm{cm}^{-1}$), and high Curie temperature ($T_C = 858$ K) [2–5]. One of the most interesting physical phenomena associated with Fe_3O_4 is the occurrence of a metal-insulator transition at ~120 K, discovered by Verwey in 1941 and therefore known as the Verwey transition (VT), revealed by the increase in resistivity and the sudden drop in magnetization [5,6]. The VT is very sensitive to stoichiometry variations, stress, and magnetic disorder in the Fe_3O_4 system (more details about the VT can be found in Refs. [5,6]). Despite having profound magnetoelectronics compatible properties, Fe_3O_4 thin films have so far not been employed to their full potential. Van der Zaag *et al.* reported a spin valve employing Fe_3O_4 as the electrode material, but the small magnetoresistance in their structures left an open question regarding the quality of the Fe_3O_4/MgO structures [7]. Later, Kado *et al.* reported magnetic tunnel junctions using Fe_3O_4/MgO layers and evidenced 26% magnetoresistance, which is, however, quite low considering the half-metallic nature of Fe_3O_4 [8]. A snag with Fe_3O_4 thin films is that during film growth, ionic disorder at the tetrahedral and octahedral sites in the crystal structure gives rise to antiphase boundaries (APBs) [9,10]. Margulies *et al.* first reported an anomalous magnetic behavior of Fe_3O_4 thin films, which was linked to the APBs [9]. The APBs induce a random magnetization distribution in zero field, and very large saturation fields. They concluded that the APBs result from the intrinsic nucleation and growth mechanism. The presence of APBs degrades both the electronic and magnetic properties, e.g., by altering the half metallicity, by increasing the resistivity, and by delaying the approach to saturation due to strong antiferromagnetic (AF) interaction across boundaries [9–13]. The APBs are abundant in epitaxial Fe_3O_4 thin films grown on MgO substrates, and the strength of the associated AF interaction depends on the angle between neighboring antiphase domains [10,14–16]. In the presence of APBs, the magnetic domain size D exhibits a $D \propto \sqrt{t}$ dependence with the thicknesses (t) of the film. Therefore, APBs are quite prominent in the thinner films and, consequently, those films require larger saturation fields [14,15]. Typically, APBs are observed as regions where the periodicity of the merging nuclei is disrupted; therefore the APBs can more broadly be described by the 1/4[110], 1/2[100], and 1/4[101] crystallographic shifts. The proportion of the APBs is about 38%, 1%, and 61% for the 1/4[110], 1/2[100], and 1/4[101] shifts, respectively [16].

Eerenstein *et al.* reported that APBs are diffusive in nature [14] since the free energy of APB-dominated thin films is higher than for APB-free films, making them unstable. Consequently, annealing of these films results in the migration of

---

[*] ankit.kumar@angstrom.uu.se

[†] peter.svedlindh@angstrom.uu.se

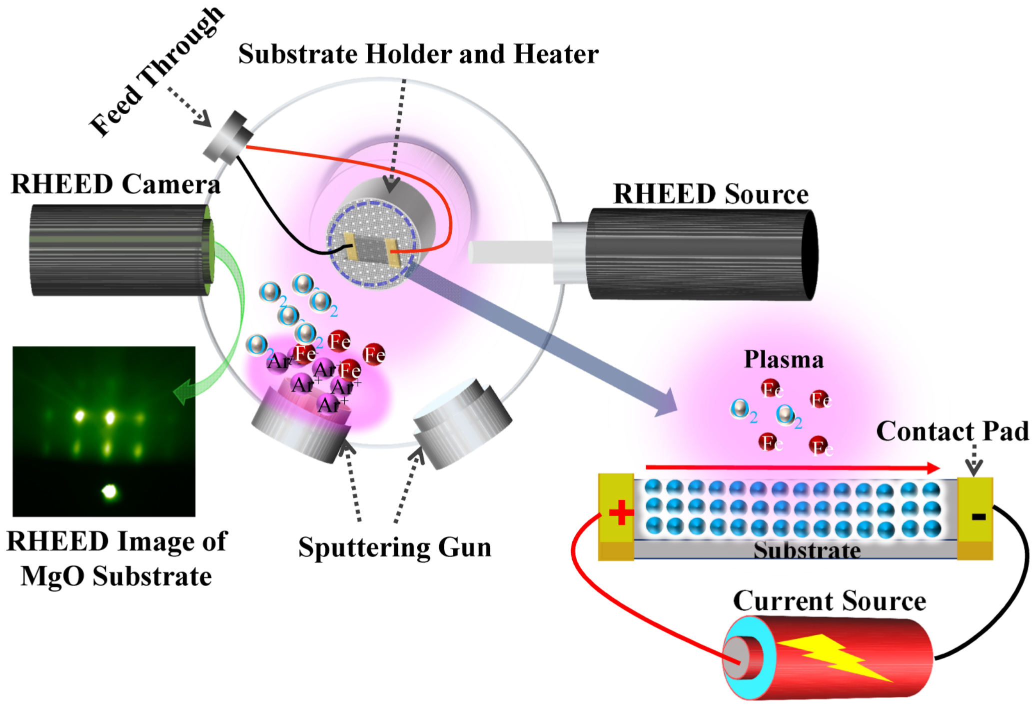

FIG. 1. Schematic layout of in-plane *in situ* electric-field-assisted pulsed dc sputter deposition of Fe_3O_4 thin films.

APBs. High-temperature growth has the potential to reduce their density [12]. At high growth temperature or when the temperature of the MgO/Fe_3O_4 film is raised, an interdiffusion of Mg and Fe cations takes place, and this interdiffusion results in a substitution of octahedrally coordinated Fe with Mg within the thin film. Therefore, Mg that segregates from the MgO substrate has a drastic effect on the surface structure and morphology and, consequently, on the electronic and magnetic properties of Fe_3O_4 [17]. Since MgO is one of the outstanding barrier materials in magnetic tunneling junctions, the growth of half-metallic (100% spin polarization) thin films over barrier materials such as MgO materials is a key ingredient in spintronic devices. The lattice mismatch between MgO ($a = 4.212$ Å) and Fe_3O_4 ($a = 8.396$ Å) is ~0.33% and has been used extensively to grow epitaxial films by various deposition techniques [10,14,18–21], however without significantly reducing the density of the APBs in the films.

Pulsed dc sputtering involves low-energy sputtered species and is not expected to provide significant adatom mobility, like other deposition methods, and thereby not favoring the migration of APBs. However, by applying an in-plane *in situ* electric field during film deposition, the electrostatic force provided by the electric field can change the surface adsorption and adatom kinetics on the substrate surface, which may result in a reduction of APBs that forms during the coalescence of nuclei in the growing film. In this paper, we report the effect of using an in-plane *in situ* electric field during low-temperature growth of epitaxial $Fe_3O_4(100)$ thin films on MgO(100) substrates on the density of APBs. The *in situ* electric field results in a rearrangement of APBs along with the formation of nanocrystallinity, in such a way that boundaries with strong AF coupling which yield a delayed saturation of the magnetization and reduced remanent magnetization are suppressed.

II. EXPERIMENTAL METHODS

Epitaxial Fe_3O_4 thin films were grown on MgO(100) substrates using pulsed dc reactive sputtering. Prior to Fe_3O_4 deposition, the MgO surface was cleaned by vacuum annealing and monitored by reflection high-energy electron diffraction (RHEED). The Fe_3O_4 phase purity was optimized by varying the oxygen partial pressure from 1.5 to 3.5×10^{-5} Torr in steps of 0.5×10^{-5} Torr, keeping constant substrate temperature, $T_S = 300\,^{\circ}\mathrm{C}$, and sputter power (85 W). The growth rate was maintained at 5.8 nm/min. In contrast to the conventional method to grow phase pure epitaxial Fe_3O_4 on MgO, we have employed a low substrate temperature (T_S) to prevent the interface diffusion which is quite prominent around and above $T_S = 400\,^{\circ}\mathrm{C}$. The film deposited at 2×10^{-5} Torr oxygen partial pressure exhibits the pure Fe_3O_4 phase, and is referred to as the as-deposited (ASD) sample. The thickness of the ASD film was 35 nm. During the process of *in situ* electric-field-assisted growth optimization, different voltages (1, 10, and 100 V) were applied between two presputtered gold contacts on the MgO(100) substrate with a gap of 6 mm. Optimized conditions were obtained for 10 V potential difference, which was chosen for a detailed study where another set of Fe_3O_4 films was deposited in the presence of the *in situ* electric field. The other growth parameters were kept the same as for the ASD sample. It is important to note that the *in situ* electric field did not change the temperature of the growing film. Figure 1 shows a schematic of the setup used for *in situ* electric-field-assisted growth of epitaxial Fe_3O_4 thin films in an ultrahigh-vacuum chamber equipped with a differentially pumped high-pressure RHEED system [12]. Two electric-field-assisted thin films with thickness 20 and 30 nm were deposited, named hereafter as ED1 (20 nm) and ED2 (30 nm), respectively.

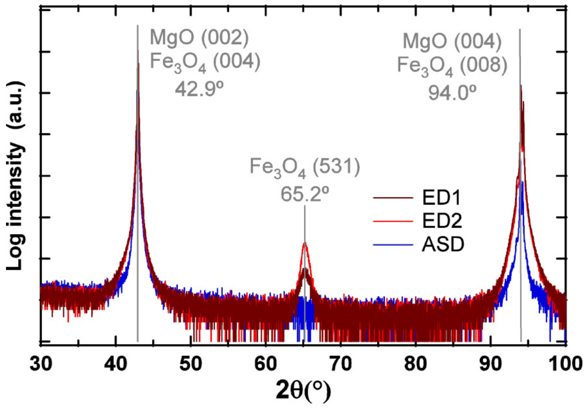

FIG. 2. $\theta/2\theta$ patterns for the ASD, ED1, and ED2 epitaxial $Fe_3O_4(100)/MgO(100)$ thin films.

X-ray diffraction $\theta/2\theta$ and pole-figure measurements were performed employing a PANalytical MRD instrument using a Cu-K_α radiation source and parallel beam optics. The measurements were conducted using a parallel plate collimator with a 0.18° acceptance angle, and a flat graphite monochromator on the secondary side (to suppress the fluorescence). In the $\theta/2\theta$ measurements, line focus and a Goebel mirror were used on the primary side, and pole figures were acquired using point focus and a poly-capillary x-ray lens on the primary side. The pole figures were measured using the $Fe_3O_4(311)$ reflection at $2\theta = 35.42°$, which also detects the tail of the MgO(111) reflection centred at $2\theta = 36.95°$.

Bright- and dark-field transmission electron microscopy (TEM) images were taken using a JEOL JEM-2100F field emission gun microscope (point resolution = 1.9 Å, $C_s = 0.5$ mm, $C_c = 1.1$ mm) equipped with a Gatan Ultrascan 1000 and a Orius 200D camera. The samples were prepared by dissolving the MgO substrate in 6 wt% ammonium sulfate solution (72 h, at 20 °C), thus under slightly different conditions as those described in Eerenstein *et al.* [14,18]. After dissolution of the MgO, the thin films were placed on carbon mesh films.

A Renishaw InVia micro Raman setup using a 532 nm laser and 1800 lines/mm grating was used to record the Raman spectra on all the samples at 2 mW power. Lower laser intensities down to 100 μW were also used to double check that no laser-induced changes of the samples occurred. Isothermal magnetizations (M) versus field (H) as well as magnetization versus temperature (T) measurements were performed on all samples using a Quantum Design MPMS system.

III. RESULT AND DISCUSSION

To confirm epitaxial growth and crystallographic orientation relationships of the Fe_3O_4 thin films deposited on MgO(100) substrates, x-ray diffraction $\theta/2\theta$ and pole-figure measurements were performed. X-ray diffractograms are shown in Fig. 2 for all samples, revealing two strong peaks situated at $2\theta = 42.9°$ and 94.0°, respectively. These two Bragg peaks perfectly match the (002) and (004) Bragg reflections of the MgO substrate [22]. They do, however, also almost match the expected positions of the (004) and (008) Fe_3O_4 reflections [14,20,23]. The absence of any clear shoulder that can be attributed to the Fe_3O_4 thin film indicates a strained epitaxial cube-on-cube growth, but it cannot be proven from the present data. The overlap also makes the exact determination of the lattice parameter for the Fe_3O_4 thin phase impossible. Conversely, it is important to mention here that the presence of APBs in epitaxial $Fe_3O_4(100)/MgO(100)$ results in compressive stress (more details are given in Ref. [19] and references therein) [19,24]. Furthermore, the ED1 and ED2 peak intensities are a bit smaller, which could be due to instrument geometry misalignment or smaller film thickness. The ED1 and ED2 films exhibit an additional weak signature at 65.2° corresponding to the $Fe_3O_4(531)$ reflection, but the concentration of crystallites with this particular orientation is roughly three orders lower than that of crystallites with the (400/800) orientations parallel to the substrate. The presence of this minute misorientation and the formation of nanocrystallinity [see Fig. 4(e)] in ED films can be linked to the electric-field-assisted growth [19]. Since the presence of APBs in epitaxial $Fe_3O_4(100)/MgO(100)$ yields compressive strain, the *in situ* electric-field-assisted migration/rearrangement of APBs results in strain relaxation, which in turn results in the observed misorientation in ED films.

To further confirm the epitaxial and/or orientation relationship pole figure, analyses were performed using the $Fe_3O_4(311)$ reflection, as shown in Figs. 3(a)–3(c) for the ASD, ED1, and ED2 films, respectively. As inferred from the pole figures, all films exhibit similar patterns that correspond to the epitaxial relationship Fe_3O_4 (001)[110] // MgO (001)[110], i.e., cube-on-cube growth. Both peaks at the out-of-plane tilt angles $\psi = 25°$ and 73° originate from the $Fe_3O_4(001)$ orientation. The narrow peaks at $\psi = 55°$ originate from the

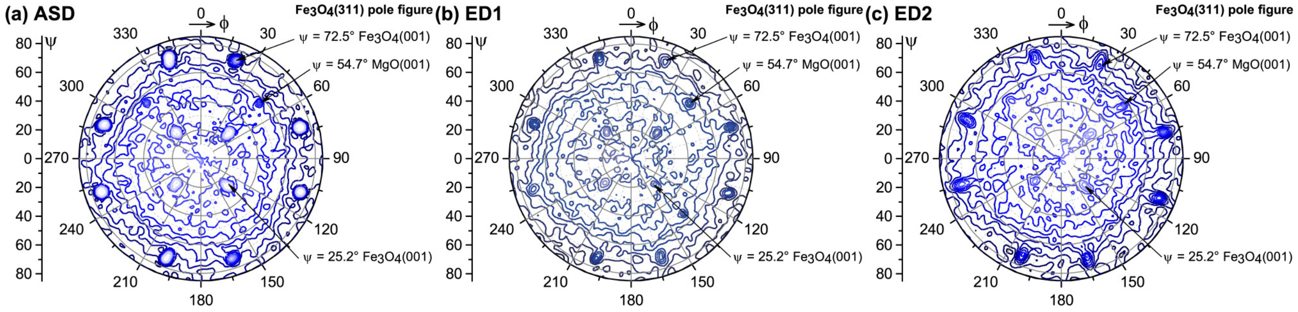

FIG. 3. Pole figures for the different samples: (a) ASD, (b) ED1, and (c) ED2. Peaks corresponding to (001) oriented Fe_3O_4 crystals visible at tilt angles (ψ) 25.2° and 72.5°; peaks from MgO(111) reflections, corresponding to the (001) oriented MgO substrate, visible at $\psi = 54.7°$.

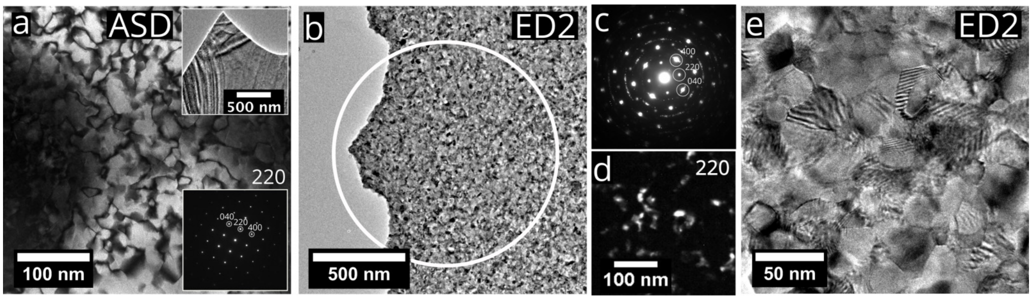

FIG. 4. Dark- and bright-field TEM images of the ASD and ED2 samples. (a) Dark-field image ([001]-zone axis) of the ASD sample. The image was formed using 220 reflection (marked by the diffraction pattern in the lower inset) to visualize the antiphase boundaries in the single-crystalline Fe_3O_4 film. The dark contrast bands at the image border are due to a slight bending of the freestanding film as also evident in the bright-field image shown in the upper inset. (b) Bright-field image of the ED2 sample. (c) Diffraction pattern corresponding to the area in the white circle in (b). (d) Dark-field image, taken using the 220 reflection in the diffraction in (c). (e) Detail of the grain structure in the ED2 film.

substrate and match the angle between the MgO(002) and MgO(111) reflections, of which the tail of the latter is detected in the present pole-figure measurements, thus confirming the in-plane relationship between the substrate and film. The minority orientation corresponding to $Fe_3O_4(531)$ observed for the electric-field-assisted deposited films is not detected in the pole figures, thus implying that the misorientation exists only in a minute amount.

Figure 4(a) shows the dark-field transmission electron microscope (DFTEM) image of the ASD sample. Imaging the sample using the weak 220 reflection [see selected area electron diffraction (SAED) pattern in the lower inset] reveals the APBs in the single-crystalline Fe_3O_4 thin film, with a domain size comparable to those observed in previous studies [10,14,18]. Figure 4(a) (upper inset) shows a bright-field image of the ASD film, which confirms the single-crystal growth as is also evident from the SAED pattern (lower inset). The presence of the slight diffraction contrast in the ASD bright-field image is due to bended contours/crystals. In contrast, the bright-field image of the ED2 sample shown in Fig. 4(b) reveals a nanocrystalline microstructure, albeit with a strongly textured electron diffraction pattern [see Fig. 4(c)]. The contrast in the ED2 DFTEM image shown in Fig. 4(d) displays diffraction contrast due to small misalignment of the nanocrystal grains, but lacks the characteristic APB zigzag pattern seen in Fig. 4(a). Indeed, at higher magnifications [Fig. 4(e)], Moiré fringes are clearly visible due to overlap between grains with similar orientation; thus, although the film is thin and strongly textured, it cannot be considered columnar.

To further confirm the phase purity, and the presence of APBs and strain in the samples, unpolarized micro-Raman measurements were performed. The Raman spectra were recorded in the 100 to 800 cm^{-1} frequency range, and only Fe_3O_4 A_{1g} and T_{2g} Raman modes were observed. Here the T_{2g} Raman active mode is triply degenerate and we are only interested in $T_{2g}(3)$, which is more sensitive to the electronic properties [4]. The recorded A_{1g} and $T_{2g}(3)$ modes for all films are shown in Fig. 5. The observed Raman spectra were fitted with a sum of Lorentzian functions, shown in Fig. 5, to extract the line-shape parameters: angular frequency (ω) and full-width at half-maximum (FWHM) linewidth (Γ). The observed values of ω and Γ are shown in Table I. The errors in obtaining Γ and ω are about 0.5 and 0.5 cm^{-1} for the A_{1g} mode and 1.5 and 0.5 cm^{-1} for the $T_{2g}(3)$ mode, respectively. The observed ω values for the A_{1g} and $T_{2g}(3)$ modes of the epitaxial films are lower than the corresponding Fe_3O_4 single-crystal values: $\omega = 668$ and 307 cm^{-1} for the A_{1g} and $T_{2g}(3)$ modes, respectively [25,26]. The ASD (35 nm) and ED2 (30 nm) films exhibit ~0% strain, respectively, whereas the ED1(20nm) film possesses ~0.38 ± 0.08% tensile strain. Here it should be stressed that the strain is the cumulative effect of the APB compressive strain, and the Fe_3O_4 and MgO lattice-mismatch-induced

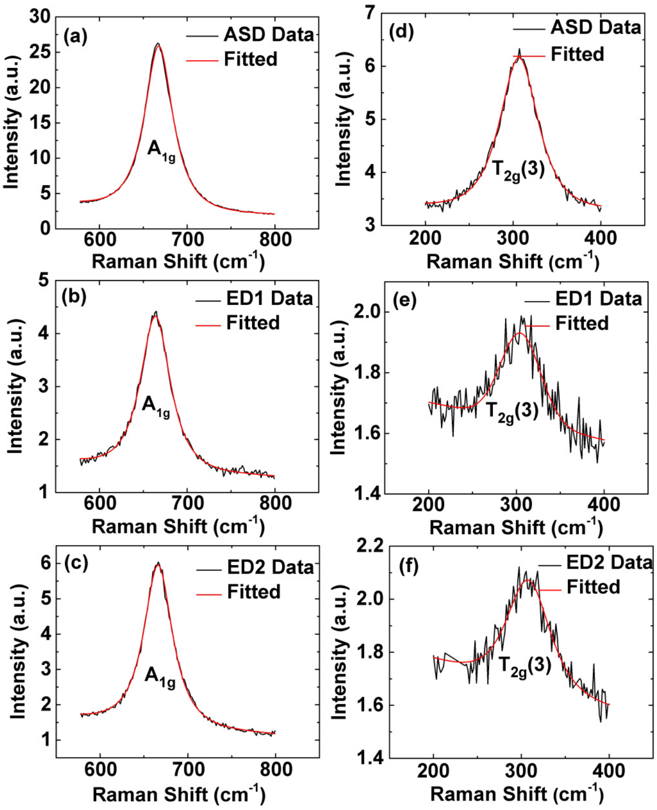

FIG. 5. Raman symmetric stretch vibration A_{1g} mode spectra for (a) ASD, (b) ED1, and (c) ED2 films, and antisymmetric and symmetric bending $T_{2g}(3)$ mode spectra for (d) ASD, (e) ED1, and (f) ED2 films. Red lines are Lorentz fits of the data to extract the line-shape parameters.

TABLE I. The Raman line-shape parameters and corresponding electron-phonon coupling strength for the different Fe_3O_4 film samples.

	A_{1g}			$T_{2g}(3)$		
Mode	ASD	ED1	ED2	ASD	ED1	ED2
$\omega(\mathrm{cm}^{-1})$	667.6	665.5	668.2	306.7	304.7	307.2
$\Gamma(\mathrm{cm}^{-1})$	37.5	39.1	37.9	50.3	53.9	55.2
λ	0.036	0.038	0.037	0.68	0.74	0.75
	Epitaxial film [4]	Single crystal [26]		Epitaxial film [4]	Single crystal [26]	
λ	–	0.045		0.72	0.51	

tensile strain. It is well known that heteroepitaxial growth of Fe_3O_4 on MgO is strained and that this strain can be accommodated until 70 nm film thickness, implying that the film is uniformly strained up to this critical thickness and that relaxation starts beyond it [19,24]. The compressive strain generated by APBs and the lattice-mismatch-induced tensile strain compensate each other to some extent and therefore allow the ASD film to grow mostly coherently/pseudomorphic with the substrate [19], which is evident from pole-figure and Raman results, in accordance with previous reports [19,24]. However, the presence of the electric field during growth provides extra kinetic energy to the adatoms in the nucleation process of the film growth and helps to reduce the density of APBs that form during the nucleation process [12,15].

To explore the presence of APBs and/or AF interactions in the samples, the Allen's approach [26,27] was employed. Originally Allen showed that the electron-phonon (*e-p*) coupling in disordered metallic systems could be estimated by the wave-vector-averaged phonon linewidth [27] since the conservation rule relaxes in the presence of disorder among different wave vectors leading to the decay of phonons into electron-hole pairs, and as a result the *e-p* interaction is enhanced [4]. This approach provides an estimation of the degree of disorder in the system by enhancing the *e-p* interaction. In epitaxial Fe_3O_4 thin films, ionic disorder results in the formation of the APBs and therefore in the enhancement of the *e-p* interactions. Moreover, the nanocrystallinity along with the small misorientation found for ED1 and ED2 can further increase the value of the *e-p* interaction. The electron-phonon coupling strength can thus be an indirect indicator of the increase in density of APBs as well as of AF interactions across grain boundaries [4]. The strength of the *e-p* coupling according to Allen's approach can be expressed for the ith phonon mode as

$$\lambda = \frac{\Gamma_i}{\omega^2} \frac{g_i}{2\pi\ N(E)}, \tag{1}$$

where g_i is the degeneracy of the ith mode, $g_i(T_{2g}) = 3$, $g_i(A_{1g}) = 1$, and $N(E)$ (= 3 states/eV per Fe at room temperature) is the density of states (DOS) at the Fermi level [4,12]. The estimated values of the *e-p* coupling strength of the A_{1g} and $T_{2g}(3)$ Raman modes are given in Table I for all the samples. In Fe_3O_4, the A_{1g} mode which is due to symmetric stretching of the oxygen atoms along the Fe-O bonds is mainly connected to structural properties, while the T_{2g} mode which is due to symmetric and asymmetric bending of oxygen with respect to Fe is linked to the electronic properties [4,28]. Therefore, growth-induced changes in the APBs are linked to the changes in the *e-p* coupling strength of the T_{2g} mode. The ASD film exhibits a lower value of $\lambda \approx 0.68 \pm 0.02$ compared to the value $\lambda \approx 0.75 \pm 0.02$ obtained for the ED1 and ED2 films. Nevertheless, the observed values of λ for films studied here are still quite low compared to previously reported values (∼0.92 or greater) for epitaxial thin films of Fe_3O_4 on MgO [29], and comparable to λ values reported for significantly reduced density of APBs in two-dimensional epitaxial Fe_3O_4 films grown on TiN buffered Si(100) [12,15]. The DFTEM image [Fig. 4(e)] reveals the absence of APBs in the ED films. Hence, the value of the *e-p* coupling constant is expected to be similar to that of bulk single-crystalline Fe_3O_4. Therefore, the small increase in λ for the electric-field deposited films compared to the ASD film can be explained by disorder at the nanocrystal grain boundaries. Here it is important to note that in our previous work [30], the *in situ* electric field was applied to the polycrystalline growth of Fe_3O_4 on naturally oxidized Si(100) substrate and, as a result, the electric-field-assisted grown film exhibited preferred oriented growth in conjunction with a significantly reduced density of APBs. The present study is different, as here the *in situ* electric field was applied during epitaxial growth of Fe_3O_4 on MgO, and APBs are typically more abundant in epitaxial films of Fe_3O_4 grown on MgO substrates.

To further investigate the effects of *in situ* electric-field-assisted growth, the results from magnetization measurements will be explored. The APBs cause AF couplings in polycrystalline (inter- and intragrain) and epitaxial (intragrain) films by superexchange interactions at the cationic/anionic sites [10,13,30]. The strength of the AF interaction depends on the relative orientation of neighboring crystallites [10,11]. Strong AF superexchange interactions at APBs exist between Fe^{3+} and Fe^{2+} ions at octahedral and Fe^{3+} ions at tetrahedral sites via O^{2-}, having 180°, 140°, and 120° angles for octahedral-O^{2-}-octahedral, tetrahedral-O^{2-}-tetrahedral, and octahedral-O^{2-}-tetrahedral couplings, respectively (for more details, see Ref. [10]). The presence of these interactions inevitably results in reduced remanent magnetization (M_r) and enlarged saturation magnetic fields ($\mu_0 H_S$), as reported previously for epitaxial growth of Fe_3O_4 thin films over MgO substrates [19]. However, interactions across APBs can also be weakly AF or even ferromagnetic (FM) in nature [10]. Magnetizations versus field measurements have been performed at different temperatures on all samples; the results are shown in Figs. 6(a)–6(c). The inset in each figure shows the temperature dependence of the saturation magnetization ($\mu_0 M_S$) estimated applying an in-plane magnetic field of 400 mT; ED films have higher $\mu_0 M_S$ compared to the ASD film. The temperature-dependent magnetic hysteresis loops of the different samples did not

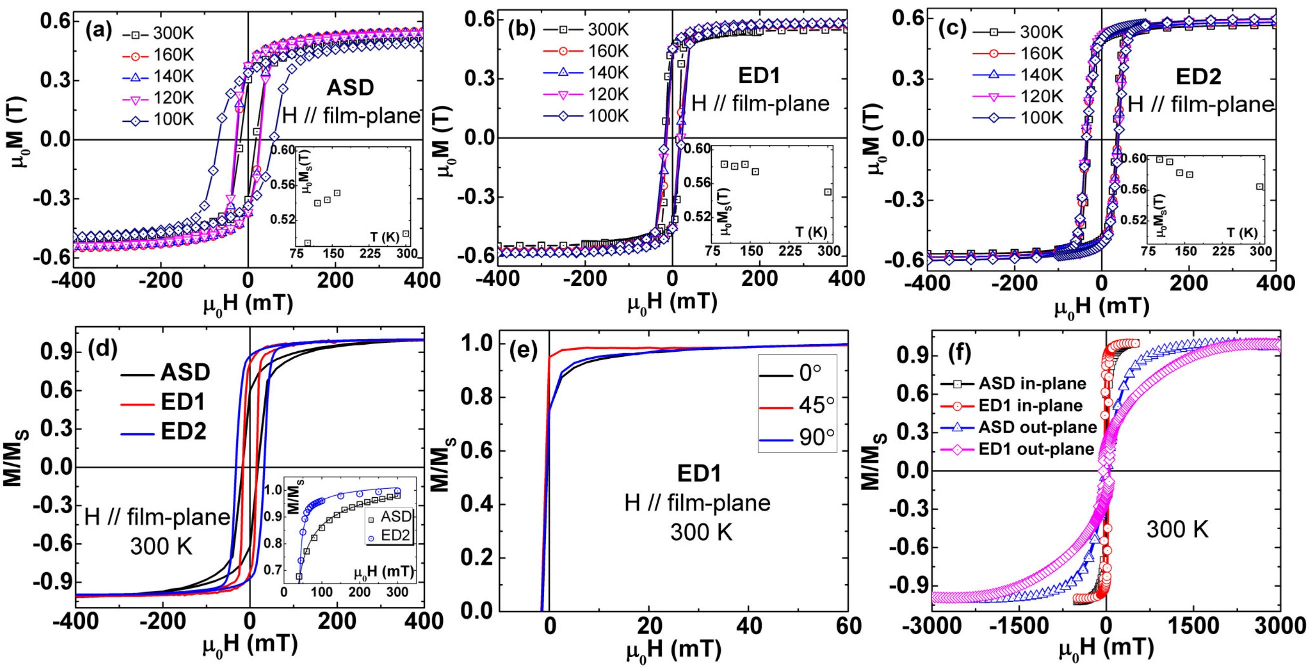

FIG. 6. In-plane magnetization vs field recorded at different temperatures for (a) ASD, (b) ED1, and (c) ED2. Insets show $M_s = M(400\ \text{mT})$ vs temperature for the different samples. It should be noted that a field of 400 mT is not enough to saturate the magnetization for the ASD sample, which becomes particularly evident at temperatures below the Verwey transition. (d) In-plane M/M_s vs field recorded at 300 K for the different samples. Inset shows a fitting using Eq. (2). (e) Magnetization vs field recorded along 0° (MgO[001]), 45° (MgO[011]), and 90° (MgO[010]) ED1 film azimuths. (f) Normalized in-plane and out-of-plane magnetization vs field for the ED1 and ASD films.

reveal any exchange bias (asymmetric hysteresis loops), which indicates that the films are devoid of strong AF interactions and pinning of uncompensated spins near APBs. The observed values of the coercivity at 300, 160, and 140 K temperatures are 17.7(33.3), 26.5(36.0), and 26.8(36.3) mT for ASD (ED2) films, respectively, while the values of the coercivity for the ED1 film are 15.8, 18.0, and 18.3 mT. A small increase in coercivity for the ED2 film compared to the ASD film, both having similar thickness, indicates that nanocrystalline grain boundaries compared to APBs are more effective in pinning domain walls. The ED1 film also exhibits a small temperature dependent increase in coercivity compared to ASD, and a low value of coercivity in the ED1 film compared to the ED2 film might be due to strain.

To be able to compare M_r and $\mu_0 H_S$ values for ASD and ED films, normalized in-plane magnetization loops measured at 300 K are shown in Fig. 6(d). The values of $\mu_0 H_S$ (M_r/M_S) for the ASD, ED1, and ED2 films are found to be 300 (61%), 150 (87%), and 150 (90%) mT, respectively. The observed values of $\mu_0 H_S$ (M_r/M_S) are quite small (large) compared to values of $\mu_0 H_S = 400$ mT ($M_r/M_S = 70\%$) reported in our previous work wherein the *in situ* electric field was applied during the polycrystalline growth of Fe_3O_4 on naturally oxidized Si(100) [30]. The dark-field TEM image for the electric-field deposited film is clearly devoid of the irregular pattern of boundaries which is characteristic of APBs. However, the dark-field image reveals the nanocrystallinity of the ED films. To estimate the density of APBs in the ASD and ED2 films, we have employed a similar approach as used by Margulies *et al.* [9] and Hibma *et al.* [31]. This approach assumes AF coupling across domain boundaries and neglects magnetocrystalline anisotropy. Accordingly, this model describes an approach to saturation of semi-infinite media separated by Bloch walls considering only competition between the Zeeman energy and the AF exchange energy. Therefore, this model provides a direct relation between the saturation behavior and the APB density, and the governing equation of this model is

$$M = M_S\left(1 - \frac{b}{(\mu_0 H)^n}\right), \tag{2}$$

where b is related to the APB density, and a value of n near 0.5 is expected for competition between exchange and Zeeman energies [9]. Fits of Eq. (2) to the magnetization versus magnetic field data of the ASD and ED2 films are shown in the inset of Fig. 6(d). The observed value of b is 0.63 (0.20) $\text{mT}^{1/2}$ for the ASD (ED2) film. The value of 0.20 $\text{mT}^{1/2}$ for b for the ED film is quite low compared to the value of 0.46 $(\text{mT})^{1/2}$ reported by Hibma *et al.* The low density of APBs in the case of the ED film results in a low value of the saturation field.

Epitaxial Fe_3O_4(110) and Fe_3O_4(111) films typically exhibit larger in-plane fourfold magnetic anisotropy compared to epitaxial Fe_3O_4(100) films, and the presence of APBs further suppresses the signature of fourfold magnetic anisotropy in Fe_3O_4(100) films [15]. The ASD film exhibits minute or insignificant in-plane fourfold magnetic anisotropy (results not shown). However, the electric-field-assisted deposited films exhibit clear evidence of fourfold magnetic anisotropy, as shown in Fig. 6(e) for the ED1 sample. However, the ED1 film exhibits a tensile stress ($\sim$0.38 ± 0.08%) and therefore a presence of uniaxial anisotropic contribution cannot be ruled out. The cubic anisotropy and the large remanent magnetization in our ED films are comparable to that obtained in Fe_3O_4 single crystals (Ref. [32] and references therein). The low $\mu_0 H_S$ and high M_r in the ED films as compared to the ASD film clearly also affirm the reduced number of APBs with strong AF exchange interactions in electric-field-assisted grown films. The applied *in situ* electric field alters the nucleation dynamics and therefore promotes the reduction of APBs. In particular, our results show that the number of APBs with strong AF interaction across the boundaries has been reduced [10,14,33]. As a result of this reduction, comparing with the results obtained for the ASD film, M_r increases while $\mu_0 H_S$ decreases. It is worth mentioning that the in-plane saturation field of the ASD film itself is quite low compared to the values reported in literature: $\geqslant$1000 mT [11,14,18–20].

The comparison of in-plane and out-of-plane magnetization loops for the ED1 and ASD films [Fig. 6(f)] reveals something unexpected (similar results are obtained for the ED2 film): the out-of-plane saturation field ($\mu_0 H_{S,\perp}$) for the ED1 film is much larger than the expected value of $\mu_0 H_{S,\perp} \sim \mu_0 M_s$. It can therefore be concluded that the ED films exhibit a strong contribution to the magnetic anisotropy favoring in-plane magnetization.

Recently, Chang *et al.* reported the dynamic atomic reconstruction growth principle for Fe_3O_4 films grown on MgO (001) substrates [34]. The x-ray absorption spectroscopy results at the Fe $L_{2,3}$ edges evidence a strong thickness dependence of the *A* (tetrahedral coordination) and *B* (octahedral coordination) site spectral weights. Bulk, APB-free Fe_3O_4 has 33% Fe^{3+} ions on tetrahedral sites, and 33% Fe^{3+} and 33% Fe^{2+} ions on octahedral sites, while in the ultrathin films, Fe^{3+} ions at tetrahedral sites are largely missing, while at the same time the amount of Fe^{3+} ions at octahedral sites is much larger than the expected 33% bulk value. This difference of Fe^{3+} ions on tetrahedral and octahedral sites balances each other with increasing thickness, and both sites approach the 33% values beyond 8 monolayers (ML) of Fe_3O_4. This MgO/Fe_3O_4 (8 ML) interface layer would reduce the positive effect of using Fe_3O_4 thin films as spin filters in spin-electronic devices and therefore acts as a magnetically dead interface. Since the oxygen sublattice is uniform in Fe_3O_4 and cationic vacancies are responsible for the APB formation, the ultrathin films reported by Chang *et al.* are expected to have a large saturation magnetic field in conjunction with low saturation magnetization and remanent magnetization, which is, however, not the case with the ED films studied here. The magnetization results presented here for the ED films suggest that a magnetically dead layer is not formed in the electric-field-assisted deposited films; however, further investigation is needed to confirm this hypothesis.

To further look into the effects of electric-field-assisted growth, field-cooled magnetization versus temperature results for the ASD and ED2 samples having comparable thickness are plotted in Fig. 7. The presence of magnetic disorder due to strong AF interactions across APBs and strain in the film can broaden and shift the Verwey transition ($T_V \sim 120$ K for single crystals) [12,24]. The Verwey transition for the ED2 sample appears approximately at 119 K, while the Verwey transition for the ASD film is in comparison sharp but shifted to lower temperature ($T_V \sim 112$ K), presumably due to the presence of magnetic disorder created by strong AF interactions across APBs [24]. The Verwey transition temperature of the ED2 film is nearly equal to the bulk value, whereas $T_V \sim 112$ K of ASD is lower due to the presence of strong AF couplings across APBs. The difference in the thermal expansion coefficient between the substrate and the Fe_3O_4 film can result in a significant change of T_V [35], which is, however, not the case for the ED2 film exhibiting a T_V of about 119 K. The Verwey also depends critically on stoichiometry [36]. A small stoichiometric variation results in a reduction of T_V along with a reduction of the drop in magnetization at T_V; however, the comparably large drop in magnetization at T_V for the ASD film rules out this possibility. The drop in the magnetization at the Verwey transition is small in the ED2 film compared to the ASD film despite $T_V \sim 119$ K. A tentative explanation for the absence of a sharp change in magnetization at T_V for electric-field-assisted grown films is the presence of large in-plane anisotropy as evidenced by the large value of the out-of-plane saturation magnetic field.

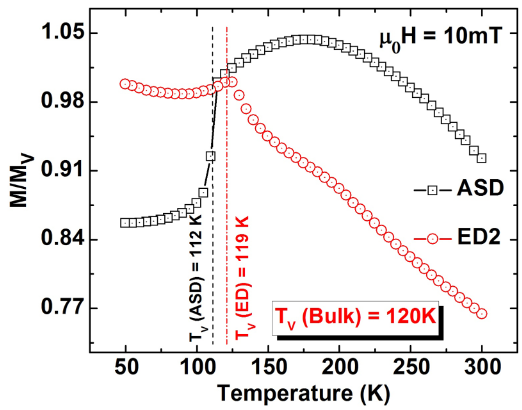

FIG. 7. Normalized field-cooled magnetization $\boldsymbol{M}/\boldsymbol{M}_V$ vs temperature to probe the Verwey transition of the ASD and ED2 samples. $\boldsymbol{\mu}_0\boldsymbol{H}$ = 10 mT and $\boldsymbol{M}_V$ is the magnetization at the Verwey transition.

In this present study, the electric field (~1.7 V/mm) was applied during growth and it is too small to modify (i) the critical barrier height for the nucleation process via the change in free energy, (ii) the surface adsorption energetics considering the incoming sputtered/atomic flux as neutral, and (iii) the surface diffusion of neutral adatoms. It can thus be concluded that the effect of the electric field on the film growth has to be electrostatic in nature, i.e., if the sputtered Fe constituents become charged as a result of interaction with the plasma, it will alter the kinetic energy of the sputtered constituents and therefore also the adsorption kinetics. Similarly, during surface jumps, the time taken by an atom could be strongly suppressed/affected if it is charged (Fe^{+3} or Fe^{+2} or O^{2-}) via the electrostatic acceleration/deceleration in the electric field, thereby affecting the nucleation process in a complex manner (due to collisions with impinging sputtered atoms/ random trajectories due to thermal effects, etc.). This we consider to be the microscopic origin of the observed difference in film growth. However, further investigations are needed to obtain a more detailed understanding of the electric-field-assisted film growth.

IV. CONCLUSION

Structural and magnetic properties of epitaxial Fe_3O_4 thin films deposited on MgO substrates by using *in situ* electric-field-assisted growth have been compared with the corresponding properties of as-deposited films. The comparison emphasizes the importance of migration and rearrangement of APBs to reduce the strength of AF interactions across these boundaries. Both ASD and ED films grow epitaxially, including ED films with minor crystallographic misorientation, with the orientational relationship Fe_3O_4 (001)[110] // MgO (001)[110]. The important effects of *in situ* electric-field-assisted growth were revealed by in-plane and out-of-plane magnetization versus field measurements. Both ED1 and ED2 exhibit a large remanent magnetization ($M_r/M_S \approx 90\%$) and small saturation field ($\mu_0 H_S \approx 150$ mT), clearly showing that the AF interactions across APBs have been greatly reduced in these films as also indirectly evidenced by the TEM dark-field images (cf. Fig. 4). Moreover, the enhanced out-of-plane saturation fields ($H_{S,\perp}$) observed for ED1 and ED2 show that the electric field induces a strong in-plane anisotropy. We would like to conclude that this innovative *in situ* electric-field-assisted growth technique will be an excellent tool for the manipulation of magnetic properties in spinel and similar systems being of importance for magnetoelectronic device technology.

ACKNOWLEDGMENTS

This work is supported by the Knut and Alice Wallenberg (KAW) Foundation Grant No. KAW 2012.0031. The KAW Foundation is acknowledged for an equipment grant for the electron microscopy facilities at Stockholm University.

---

[1] P. Tartaj, M. P. Morales, T. Gonzalez-Carreño, S. Veintemillas-Verdaguer, and C. J. Serna, Adv. Mater. **23**, 5243 (2011).
[2] Z. Zhang and S. Satpathy, Phys. Rev. B **44**, 13319 (1991).
[3] Y. S. Dedkov, U. Rudiger, and G. Guntherodt, Phys. Rev. B **65**, 064417 (2002).
[4] A. Kumar, S. Chaudhary, D. K. Pandya, and S. K. Sharma, Phys. Rev. B. **90**, 024302 (2014).
[5] F. Walz, J. Phys.: Condens. Matter **14**, R285 (2002).
[6] E. J. W. Verwey, and P.W. Haayman, Physica **8**, 979 (1941).
[7] P. J. van der Zaag, P. J. H. Bloemena, J. M. Gaines, R. M. Wolf, P. A. A. van der Heijden, R. J. M. van de Veerdonk, and W. J. M. de Jonge, J. Magn. Magn. Mater. **211**, 301 (2000).
[8] T. Kado, Appl. Phys. Lett. **92**, 092502 (2008).
[9] D. T. Margulies, F. T. Parker, M. L. Rudee, F. E. Spada, J. N. Chapman, P. R. Aitchison, and A. E. Berkowitz, Phys. Rev. Lett. **79**, 5162 (1997).
[10] S. Celotto, W. Eerenstein, and T. Hibma, Eur. Phys. J. B **36**, 271 (2003).
[11] A. V. Ramos, J. B. Moussy, M. J. Guittet, A. M. Bataille, M. Gautier Soyer, M. Viret, C. Gatel, P. Bayle Guillemaud and E. Snoeck, J. Appl. Phys. **100**, 103902 (2006).
[12] A. Kumar, D. K. Pandya, and S. Chaudhary, Appl. Phys. Lett. **102**, 152406 (2013).
[13] W. L. Zhou, K.-Y. Wang, C. J. O'Connor, and J. Tang, J. Appl. Phys. **89**, 7389 (2001).
[14] W. Eerenstein, T. T. M. Palstra, T. Hibma, and S. Celotto, Phys. Rev. B **68**, 014428 (2003).
[15] A. Kumar, S. Jana, P. Svedlindh, S. K. Sharma, S. Chaudhary and D. K. Pandya, J. Mater. Chem. C **4**, 9942 (2016).
[16] Akira Ikeuchi, Satoshi Hiura, Taichi Mizuno, Eisaku Kaji, Agus Subagyo, and Kazuhisa, Jpn. J. Appl. Phys. **51**, 08KB02 (2012).
[17] J. F. Anderson, Markus Kuhn, Ulrike Diebold, K. Shaw, P. Stoyanov, and D. Lind, Phys. Rev. B **56**, 9902 (1997).
[18] W. Eerenstein, T. T. M. Palstra, S. S. Saxena and T. Hibma, Phys. Rev. Lett. **88**, 247204 (2002).
[19] K. Balakrishnan, S. K. Arora and I. Shvets, J. Phys.: Condens. Matter **16**, 5387 (2004).
[20] F. Bertram, C. Deiter, O. Hoefert, T. Schemme, F. Timmer, M. Suendorf, B. Zimmermann and J. Wollschläger, J. Phys. D: Appl. Phys. **45**, 395302 (2012).
[21] O. Chichvarina, T. S. Herng, W. Xiao, X. Hong, and J. Ding, J. Appl. Phys. **117**, 17D722 (2015).
[22] H. E. Swanson and E. Tatge, Natl. Bur. Stand. Circ. **1**, 37 (1953).
[23] H. E. Swanson, H. F. McMurdie, and M. C. Morris, Natl. Bur. Stand. Monograph **25**, 31 (1967).
[24] S. K. Arora, R. G. S. Sofin, and I. V. Shvets, J Appl. Phys. **100**, 073908 (2006).
[25] O. N. Shebanova and P. Lazor, J. Solid. State Chem. **174**, 424 (2003).
[26] R. Gupta, A. K. Sood, P. Metcalf, and J. M. Honig, Phys. Rev. B **65**, 104430 (2002).
[27] P. B. Allen, Solid State Commun. **14**, 937 (1974).
[28] J. L. Verble, Phys. Rev. B: Solid State **9**, 5236 (1974).
[29] D. M. Phase, S. Tiwari, R. Prakash, A. Dubey, and V. G. Sathe, J. Appl. Phys. **100**, 123703 (2006).
[30] A. Kumar, D. K. Pandya, and S. Chaudhary, J. Appl. Phys. **112**, 073909 (2012).
[31] T. Hibma, F. C. Voogt, L. Niesen, P. A. A. van der Heijden, W. J. M. de Jonge, J. J. T. M. Donkers, and P. J. van der Zaag, J. Appl. Phys. **85**, 5291 (1999).
[32] Ö. Özdemir, and D. J. Dunlop, Earth Planet. Sci. Lett. **165**, 229 (1999).
[33] K. P. McKenna, F. Hofer, D. Gilks, V. K. Lazarov, C. Chen, Z. Wang and Y. Ikuhara, Nat. Commun. **5**, 5740 (2014).
[34] C.F. Chang, Z. Hu, S. Klein, X.H. Liu, R. Sutarto, A. Tanaka, J.C. Cezar, N.B. Brookes, H.-J. Lin, H.H. Hsieh, C.T. Chen, A.D. Rata, and L.H. Tjeng, Phys. Rev. X **6**, 041011 (2016).
[35] P. J. van der Zaag, W. F. J. Fontijn, P. Gaspard, R. M. Wolf, V. A. M. Brabers, R. J. M. van de Veerdonk, and P. A. A. van der Heijden, J. Appl. Phys. **79**, 5936 (1996).
[36] R. Aragon and D. J. Buttrey, John P. Shepherd, and Jurgen M. Honig, Phys. Rev. B **31**, 430 (1985).